Influences of different barrier films on microstructures and electrical properties of Bi_2Te_3-based joints

Jinxuan Cheng[1] · Xiaowu Hu[1] · Qinglin Li[2]

Abstract

Diffusion barrier film was strongly proposed to utilize in Bi_2Te_3-based thermoelectric (TE) module. However, effects of different barriers on microstructures of solder joints and electrical properties of TE modules were still unclear, which were vital in practical applications. In current work, Bi_2Te_3-based TE modules without barrier (TM), with Ni (TM_{Ni}) and with Ni/Au ($TM_{Ni/Au}$) were fabricated via reflow-soldering. Experimental results revealed that at the interface between SAC305 solder and P- or N- type Bi_2Te_3 sample, the Ni or Ni/Au barrier could efficiently inhibit severe growth of the intermetallic compound (IMC) phase. Remarkably, a thinner IMC layer was observed at the solder/Au/Ni/Bi_2Te_3 interface, which was attributed to effects of Au elements on suppressing the formation of IMCs. The results of power generation ability test revealed that TM_{Ni} exhibited higher value of output power (P) under the temperature difference (ΔT) due to its higher values of open circuit voltage (V) and output current (I). On the other hand, since the lowest electrical resistance (R) and relatively low output current of $TM_{Ni/Au}$ were measured during the test, the $TM_{Ni/Au}$ was suggested to generate less heat, meaning it consumed less energy, and hence be theoretically more efficient in improving the conversion efficiency.

1 Introduction

For sake of environmental protection, the massive use of nonrenewable sources, such as coal, natural gas and oil, was gradually reduced with the rapid development of green technology [1–3]. Significantly, exploiting renewable and eco-friendly energy was one of the highly important and necessary methods. As a promising solution, developing thermoelectric generators (TEGs), which could harvest the thermal energy scavenged from many abandoned sources and convert it into electricity, has attracted widespread concern [4–8]. Hence, plenty of exploration projects on designing and improving TE devices were carried out in research works [9–15]. For instance, Torfs et al. have invented an autonomous wearable pulse oximeter, which was operated by the BiTe-based TE system and could efficiently control oxygen saturation under the temperature difference between the body surface and ambient temperature [16]. And in the medical field, Jaziri et al. have presented a TEG model to ideally replace the implantable common medical devices whereas the task of maintaining the rechargeable batteries was arduous and time-consuming [17]. Moreover, some automotive industries have focused on designing TEGs to utilize the wasted heat from the exhaust gas, and turn it into electrical energy to power vehicles [18–20].

As a vital part of the TEG system, TE materials mainly included the following three categories: polymers, ceramics and semiconductors. In previous researches, the polymers and ceramics have been widely studied due to nontoxic, high chemical stability and low cost. Typically, Wang et al. have investigated the effect of the multiwalled carbon nanotube composites in polythiophene on the TE performance and obtained the maximum ZT value of 8.71×10^{-4} [21]. Kim et al. have studied the TE property of poly (3,4-ethylenedioxythiophene)/ styrenesulphonate and reported the ZT value of 0.42 at the ambient temperature [22]. Zhu et al. have examined the effect of Dy or Yb dopant on $CaMnO_3$ ceramics on the TE performance at 973 K. It was depicted that the maximum $ZT = 0.21$ was obtained by means of the appropriate Dy and Bi doping [23]. As aforementioned earlier, though much effort was made to enhance the properties of these materials,

✉ Xiaowu Hu
huxiaowu@ncu.edu.cn

1　School of Mechanical & Electrical Engineering, Nanchang University, Nanchang 330031, China

2　State Key Laboratory of Advanced Processing and Recycling of Nonferrous Metals, Lanzhou University of Technology, Lanzhou 730050, People's Republic of China

ZT values of polymers and ceramics were still not desired nowadays. Conversely, semiconductors have been confirmed to have higher seebeck coefficients due to their high atomic weight. Especially, grand specifications such as low thermal conductivity, high conductivity and large seebeck coefficient were detected on some small bandgap semiconductors [24]. In an experiment conducted by Rhyee et al., the *ZT* for $In_4Se_{3-\sigma}$ have reported being 1.48 at 705 K, which was based on the excellent TE performance in the charge density wave plane [25]. Zhao et al. have obtained the *ZT* of 2.6 at 923 K for the single crystal semiconductor material, SnSe [26]. And in the lower temperature condition, Bi_2Te_3-based semiconductors were considered as the more reliable materials in the fabrication of TE devices [27–29]. Generally, *ZT* values of commercial Bi-Te based alloys were closed to unity [30]. Furthermore, Through low temperature metal organic chemical vapor deposition (MOCVD) process, the P-type $(Bi,Sb)_2Te_3$ alloy could yield the $ZT_{@300 K}$ of 2.4 [31]. Thus, most of TE applications working at room temperature were powered by the Bi-Te-based TEGs nowadays.

Generally, most TE devices always worked under combined effects of a series of TE modules. Each module was mainly fabricated by connecting P- and N- type TE materials with copper or other metal electrodes, and then sandwiched using two dielectric substrates with high thermal conductivity. Thus, the efficiency of TE module depended not only on the inherent performance of TE materials, but also on properties of solder joints between TE and electrodes. Commonly, the intermetallic compound (IMC), which formed at the joint interface, was confirmed to degrade the strength and electrical conductivity of the solder joint, and hence caused underestimation of the efficiency of TE generators [32–34]. And in Chen's work, the similar conclusion, where contact resistance was considered to play an important role in improving the properties of TE module, has been drawn [35]. To cope with the issue, the introduction of diffusion barrier at the joint interface has been proposed [36,37]. Hsieh et al. have reported that electroless Co-P layer could significantly inhibit the interdiffusion in the Ni(Cu)/PbTe joints [38]. Ren et al. have investigated the effect of Au addition on the Bi_2Te_3-based joint interface, and suggested that the responsivity and photoconversion efficiency were greatly enhanced [39]. Also, other studies have reported that some elemental additions, such as Au [40], Ag [41] and Te [42], were significant in improved the thermoelectric properties of Bi_2Te_3-based module. Based on previous mass researches, in our investigation, effort was made to explore an appropriate diffusion barrier which could improve the microstructure of Bi_2Te_3-based joint interface, and consequently enhance the reliability of solder joints. As well as, according to the experimental data, the electrical properties and conversion efficiency of TE modules with various diffusion barriers would be comprehensively evaluated.

2 Experimental procedures

2.1 The process of the TE module fabrication

The P- and N- type Bi_2Te_3 bulks were supported by the commercial vendor (NanChang Hanchen New Materials Technology Co., Ltd, China). According to the information provided by the supplier, these two types of TE bulks were synthesized by ball-milling/hot pressing method using different powders balanced by atomic ratio (P-type Bi_2Te_3: $Bi_{0.5}Sb_{1.5}Te_3$; N-type Bi_2Te_3: $Bi_2Se_{0.15}Te_{2.85}$), meantime, to ensure that no impurities were introduced, the whole preparation process was conducted in an ultra-high vacuum. And the details of this method have been described in our previous work [43].

Two types of TE bulks were cut to pieces with dimensions of $2 \times 10 \times 10$ mm^3 by using a wire electrical discharge machine (DK7745), and these samples were grinded and polished. Then, the electroplating solution was used to prepare nickel coating, and appropriate formulas of solution were listed in Table 1. To enhance the adhesion of electroplated Ni layer on the surface of TE sample, during the whole plating process, each sample was completely immersed into the plating solution at 40 °C, and the current density was controlled within a range of 16–20 mA/cm^2 for 8 min. To obtain the Ni/Au barrier, the ion sputtering apparatus (E-1045) was used to sputter a thin Au layer (40 nm) on the Ni-coated Bi_2Te_3 specimen.

To connect the P- and N-Bi_2Te_3 specimens in order with copper electrodes, the Sn3.0Ag0.5Cu solder (SAC305, provided by Shenzhen Kellyshun technology Co., Ltd) was pasted on the specimens in advance, and then welded via using the reflow furnace (TYR108N-C). It was noted that nitrogen served as a shielding gas to protect alloys from oxidation during reflow-soldering. After soldering at 260 °C for 3 min, Bi_2Te_3-based TE modules without barrier (TM), with

Table 1 Compositions of electroplating bath for Ni

Components of plating bath	Concentration
$NiSO_4 \cdot 6H_2O$	280.00 (g/L)
$NiCl_2 \cdot 6H_2O$	35.04 (g/L)
H_3BO_3	32.05 (g/L)
SDS ($C_{12}H_{25}SO_4Na$)	0.04 (g/L)
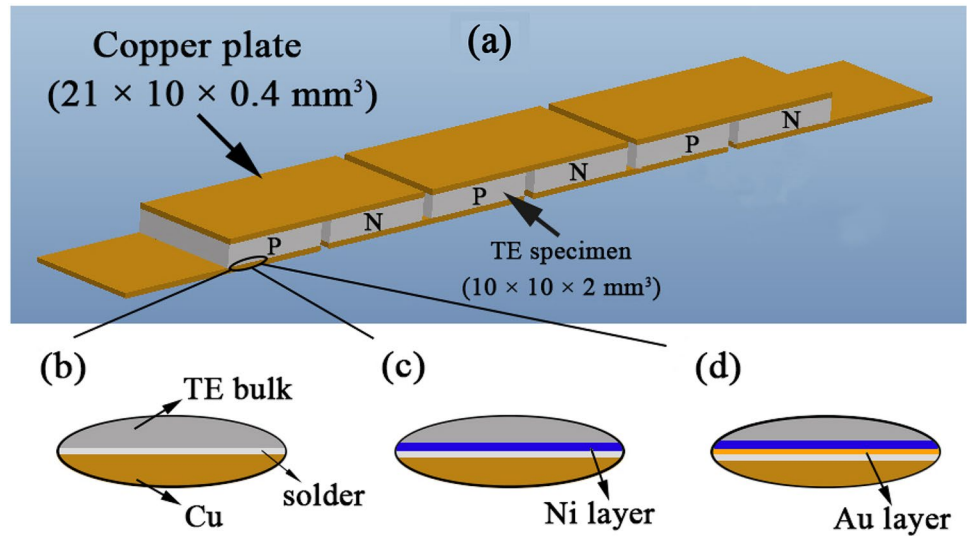
Ni (TM$_{Ni}$) and with Ni/Au (TM$_{Ni/Au}$) were established, and the schematic was shown in Fig. 1a–d.

2.2 Characterization and thermoelectric power generation measurement

To study influences of barriers on the growth of IMC layers, the scanning electron microscope (SEM, FEI Quanta 200F) was used to observe the interfacial microstructure of

all TE modules with various barrier layers. To ensure that the SEM images were clear and distinct, the SEM analysis was performed at a voltage of 30 kV and the detection was performed under high vacuum. Moreover, energy dispersive spectrum (EDS) and electron probe microanalysis (EPMA) were used to detect the distribution of dominated elements.

As shown in Fig. 2a–e, to make the temperature difference (ΔT) between the bottom and top of the TE module, an electrical heating platform (MT-2020) was used to control the temperature on the hot side, while the temperature of cold side was maintained at ~3.2 °C by using the ice-water

Fig. 2 a Apparatus and materials prepared for the experiment; **b** The schematic structure of experimental system; **c** The image of TE modules (3 pairs) under temperature difference; **d** The real-time temperature of the cold side; **e** The real-time temperature of the hot side
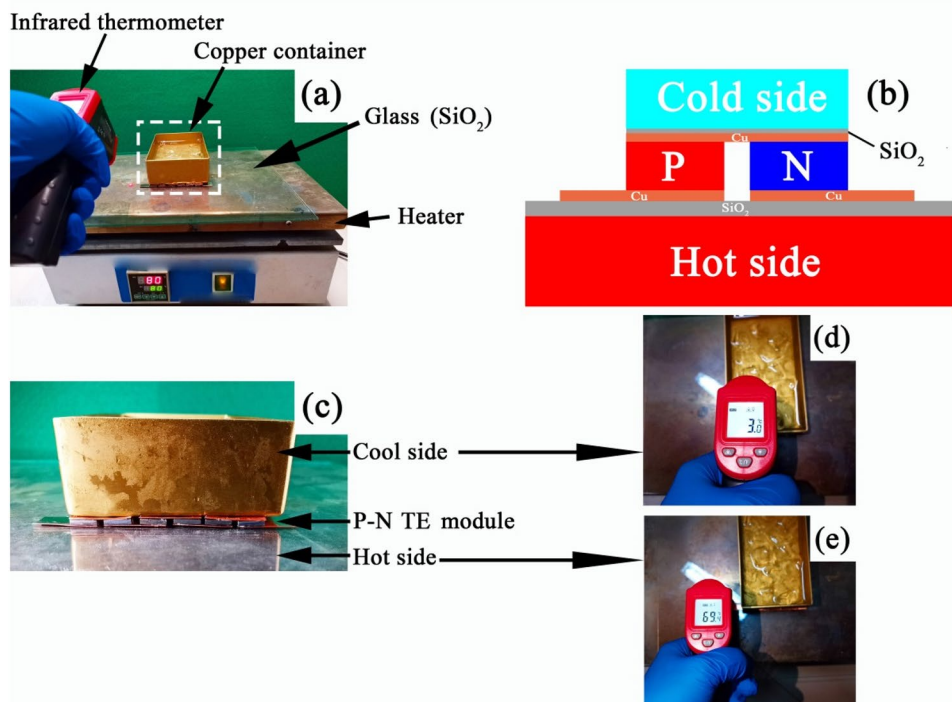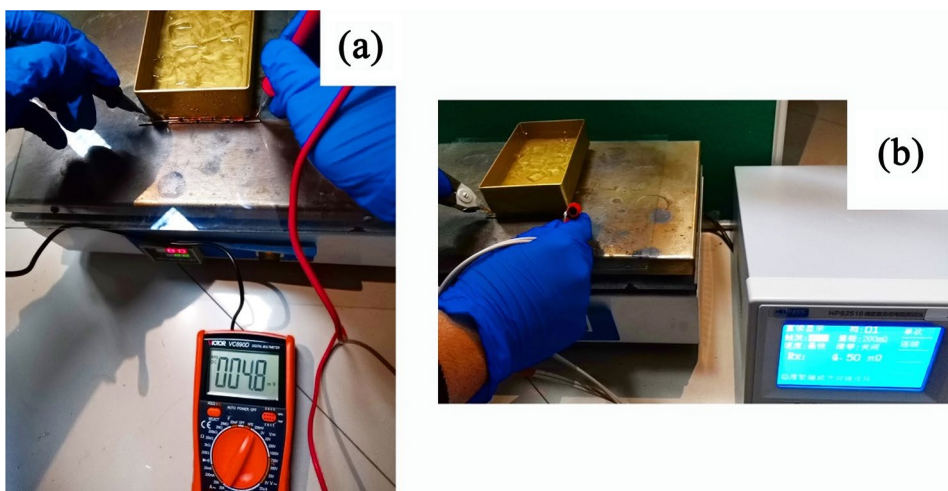
Fig. 3 Equipment prepared for measuring **a** the open circuit voltage, output current and **b** electrical resistance

mixture (the room temperature was 14 °C). Notably, thin dielectric substrates (SiO$_2$) and the TE module were held in place by the thermal conductive silicone, as illustrated in Fig. 2b. In Fig. 3a, b, the open circuit voltage (*V*) and output current (*I*) of TE module under different ΔT were measured using the multimeter (VC890D), while DC resistance tester (HPS2510A) was used to measure the electrical resistance (*R*) of TE module.

3 Results and discussions

3.1 Interfacial reaction in the Cu/SAC305/P-Bi$_2$Te$_3$ couple

Figure 4a showed the cross-sectional SEM micrograph of the Cu/SAC305/P-Bi$_2$Te$_3$ interface. After reflowing at 260 °C for 3 min, it was obvious that a continuous IMC layer with thickness of 1–3 µm formed at the Cu/SAC305 interface. Prakash et al. have studied the growth mechanism of Cu-Sn compounds, and concluded that the η-Cu$_6$Sn$_5$ phase was the preferred product at the Sn-based solder/Cu interface [44]. In addition, the Cu$_3$Sn layer was also found at the interface and mainly controlled by volume diffusion, but in this
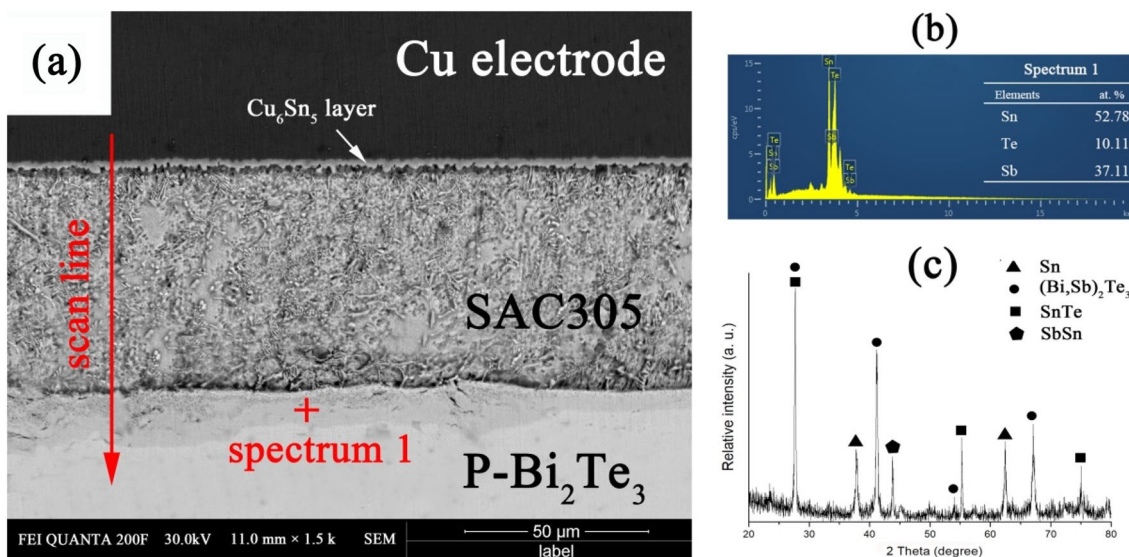

Fig. 4 a The cross-sectional SEM micrograph of the Cu/SAC305/P-Bi$_2$Te$_3$ interface after reflow-soldering at 260 °C for 3 min; **b** The EDS result of spectrum 1; **c** The XRD results of SAC305/P-Bi$_2$Te$_3$ interface

study, due to the short time for liquid solder solidification, the Cu_3Sn phase could not be detected and the IMC layer was mainly composed of Cu_6Sn_5 phases. At the SAC305/P-Bi_2Te_3 interface, another continues IMC layer was also observed to unevenly form, and the average thickness was 12–15 µm. Its composition was determined to be 52.78 at.% Sn, 10.11 at.% Te and 37.11 at.% Sb using EDS, as shown in Fig. 4b, and XRD results in Fig. 4c shows that Sn, SnTe, SbSn and $(Bi,Sb)_2Te_3$ phases were detected at the interface between SAC305 solder and P-type substrate. Chen et al. have demonstrated that Sb atoms diffused into the SnTe layer during the reaction period, and especially concentrated on the P-Bi_2Te_3 side [35]. In an investigation conducted by Lee et al., the Sn–Te–Sb ternary system has been systematically studied, and it suggested that the growth rate of the SnTe–Sn reaction layer was significantly influenced by the Sb addition, since the SbSn phase was found to serve as nucleation agents for SnTe nuclei [45]. Furthermore, researchers had confirmed that SnTe compound was the dominated phase which had a porous microstructure, thus in the early stage of the reaction, liquid Sn phase could diffuse into the SnTe layer, and gradually solidify after reflowing [46]. So it indicated that the heterogeneous reaction layer was a SnTe + SbSn + Sn + Sb mixture at the interface.

To determine the distributions of elements at joint interfaces, element line profiles of relative elements at the Cu/SAC305/P-Bi_2Te_3 interfaces were exhibited in Fig. 5. As shown in Fig. 5a, it was clearly seen that the Sn atoms were mainly distributed in the solder after reflowing. Meantime, the content of Sn atoms was higher in the P-Bi_2Te_3 compared

that in the Cu electrode, thus it strongly confirmed the above viewpoint, in which Sn atoms were confirmed to more easily diffuse into SnTe layer, and hence reacted with Te atoms. As shown in Fig. 5b, d, the Te and Sb atoms diffused into the solder under concentration gradient, but the diffusion processes would be efficiently prevented at the Cu/solder interface. In Fig. 5c, Cu atoms were found to almost retain in the Cu electrode, which were inhibited by the Cu_6Sn_5 layer. In previous investigations, researchers have concluded that in the Sn/Cu joint system, the growth of Cu_6Sn_5 was mainly diffusion-controlled during the reflow-soldering, and with thickening of the IMC layer, dominated elements would difficultly diffuse from the grain boundaries of Cu_6Sn_5 phases due to the low concentration gradient [47–49]. Furthermore, the intensity of Cu in the solder at the position marked by the red oval in Fig. 5c indicated that Cu-Sn compounds produced in the solder matrix during the reflow-soldering.

3.2 Interfacial reaction in the Cu/SAC305/Ni/P-Bi_2Te_3 couple

Figure 6 showed the cross-sectional SEM micrograph of the Cu/SAC305/Ni/P-Bi_2Te_3 interface after reflow-soldering at 260 °C for 3 min. As shown in Fig. 6a, on the electrode side, the IMC layer with thickness of 1–3 µm was observed at the interface between the electrode and the solder, which was similar to that in Cu/SAC305/P-Bi_2Te_3 couple, suggesting that the growth rate of Cu_6Sn_5 IMC layer was not affected with the introduction of Ni barrier in this joint system. On the side of the Ni barrier,
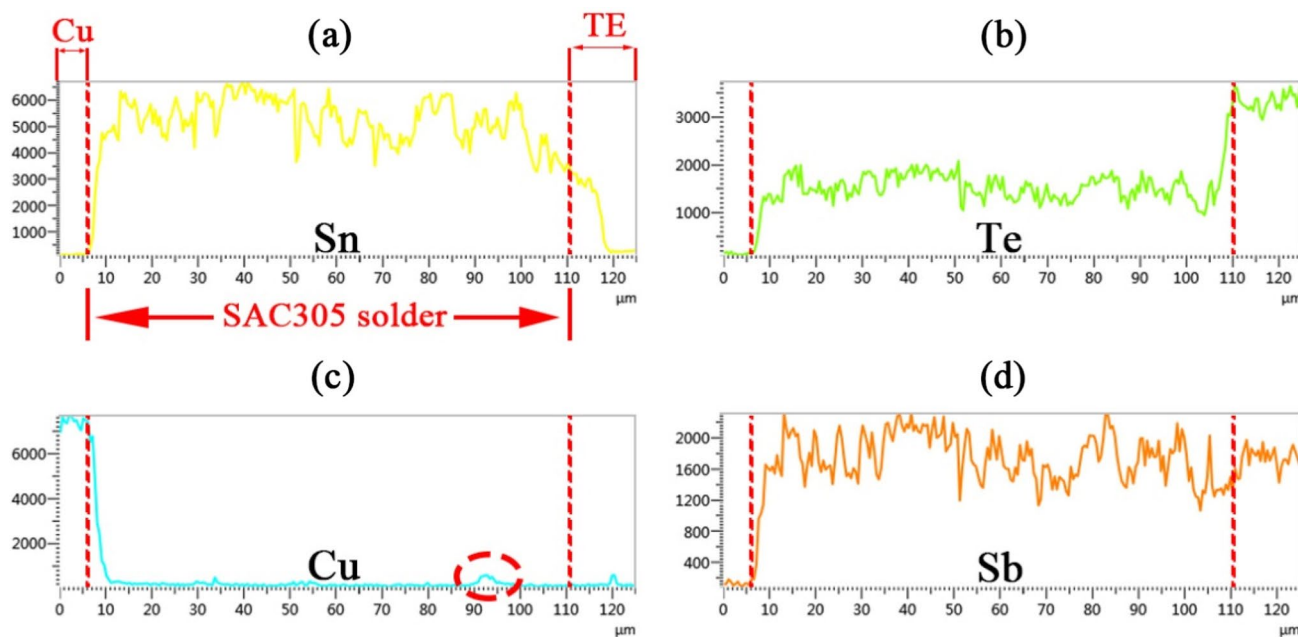

Fig. 5 Element line profiles of relative elements at the Cu/SAC305/P-Bi_2Te_3 interface in Fig. 4a. **a** Sn; **b** Te; **c** Cu; **d** Sb

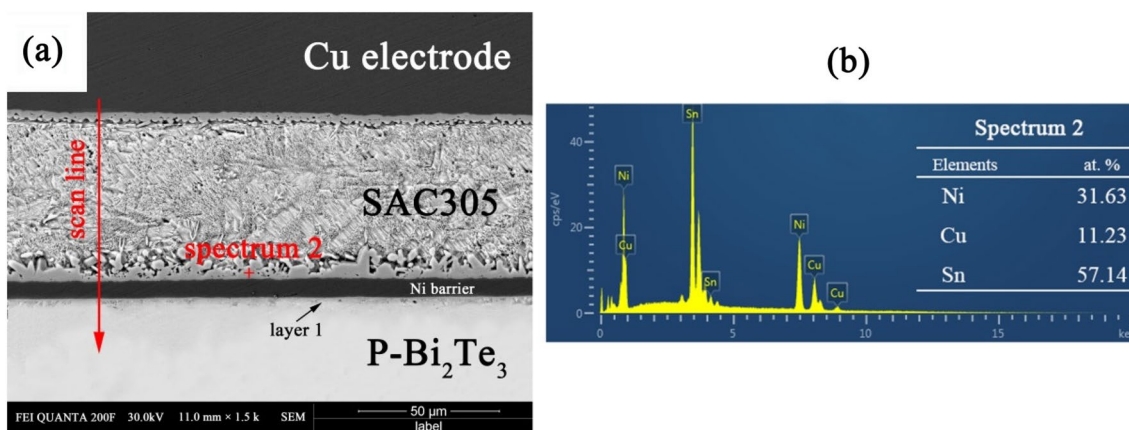**Fig. 6** **a** The cross-sectional SEM micrograph of the Cu/SAC305/Ni/P-Bi$_2$Te$_3$ interface after reflow-soldering at 260 °C for 3 min; **b** The EDS result of spectrum 2

the Ni–Cu–Sn ternary IMC was detected to form at the interface between solder and Ni barrier, and its composition was determined to be 31.63 at.% Ni, 11.23 at.% Cu and 57.14 at.% Sn, as shown in Fig. 6b. According to the Sn–Cu–Ni isothermal section, it was identified as the $(Ni,Cu)_3Sn_4$ phase [50]. Meanwhile, at the interface between the Ni barrier and P-Bi$_2$Te$_3$, another thin layer (layer 1 in Fig. 6a) was detected, which was consistence with the previous reported studies. Typically, Yusufu et al. have detected this phase using X-ray diffraction (XRD),
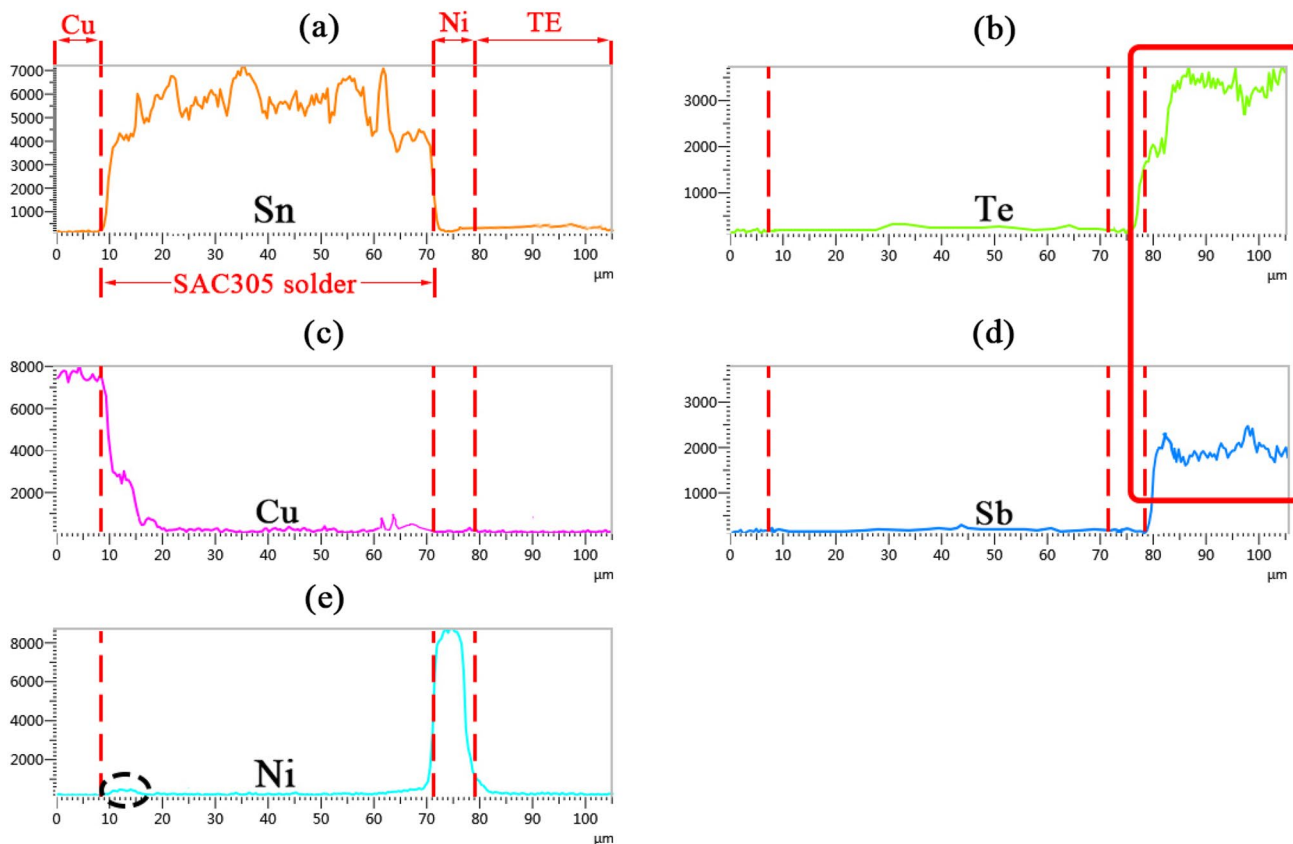

Fig. 7 Element line profiles of relative elements at the Cu/SAC305/Ni/P-Bi$_2$Te$_3$ interface in Fig. 6a. **a** Sn; **b** Te; **c** Cu; **d** Sb; **e** Ni

and suggested that it was a NiTe layer which grew at a sluggish rate at the Ni/BiTe interface [51].

Figure 7 showed element line profiles of relative elements at the Cu/SAC305/Ni/P-Bi$_2$Te$_3$ interface in Fig. 6a. As shown in Fig. 7a, it was clear that Sn atoms distributed mainly in the SAC305 solder. And the intensities of Te and Sb in the P-Bi$_2$Te$_3$ at the position marked by the red rectangle showed that these two kinds of atoms were prevented to diffuse into the solder, as shown in Fig. 7b, d. On the side of the electrode, as shown in Fig. 7c, Cu atoms mainly diffused into the solder and reacted with Sn atoms. Meanwhile, the Cu was also observed in the solder matrix, indicating that the inner reaction has occurred in the solder during the reflow-soldering. Remarkably, Ni atoms in the barrier were barely diffused into the solder or P-Bi$_2$Te$_3$, as shown in Fig. 7e. But the intensity of Ni at position marked by the black oval was detected at the interface between Cu and solder, which suggested that a tiny amount of Ni atoms dissolved into the Cu$_6$Sn$_5$. According to some literatures, the Ni addition was found to modify the scallop-liked Cu$_6$Sn$_5$ into a hexagonal rod-liked morphology, and the (Cu,Ni)$_6$Sn$_5$ has been confirmed to be thermodynamically stable phase

at the Sn-Ni-Cu system [50]. In order to examine the gradient distribution of dominated elements, EPMA results of relative atoms were presented in Fig. 8. Obviously, Sn, Te and Sb elements were efficiently separated by Ni coating, as shown in Fig. 8a–d. And in Fig. 8e, lower concentration of Cu elements has been detected on both sides of SAC305 solder, which indicated that Cu preferentially participated in the reaction during reflow-soldering.

3.3 Interfacial reaction in the Cu/SAC305/Au/Ni/P-Bi$_2$Te$_3$ couple

Figure 9a showed the cross-sectional SEM micrograph of the Cu/SAC305/Au/Ni/P-Bi$_2$Te$_3$ interface after reflow-soldering at 260 °C for 3 min. Only the Ni barrier with thickness of 5–8 μm was observed adhering to the P-Bi$_2$Te$_3$ bulk, and the Au layer was absent. It suggested that Au atoms in the sputtering layer have absolutely dissolved during the soldering. Meantime, compared with IMC layers in the other two systems, the continuous IMC layer in Cu/SAC305/Au/Ni/P-Bi$_2$Te$_3$ system was thinner. And its composition was determined to be 24.1 at. % Ni, 18.82
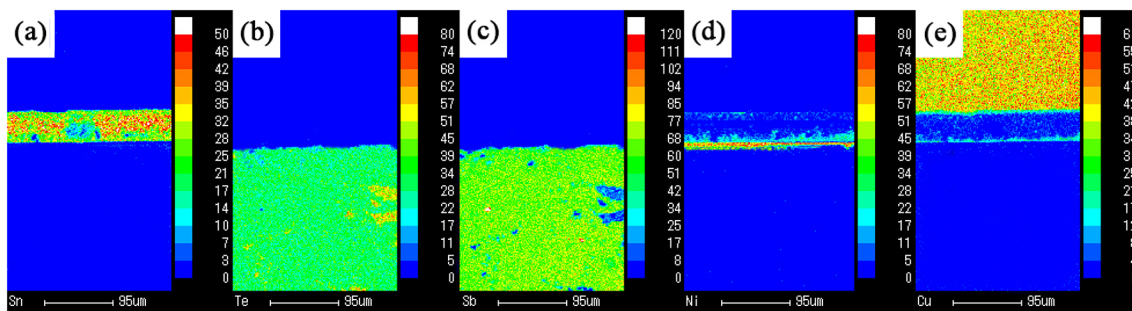

Fig. 8 EPMA results of relative elements at the Cu/SAC305/Ni/P-Bi$_2$Te$_3$ interface. **a** Sn; **b** Te; **c** Sb; **d** Ni; **e** Cu
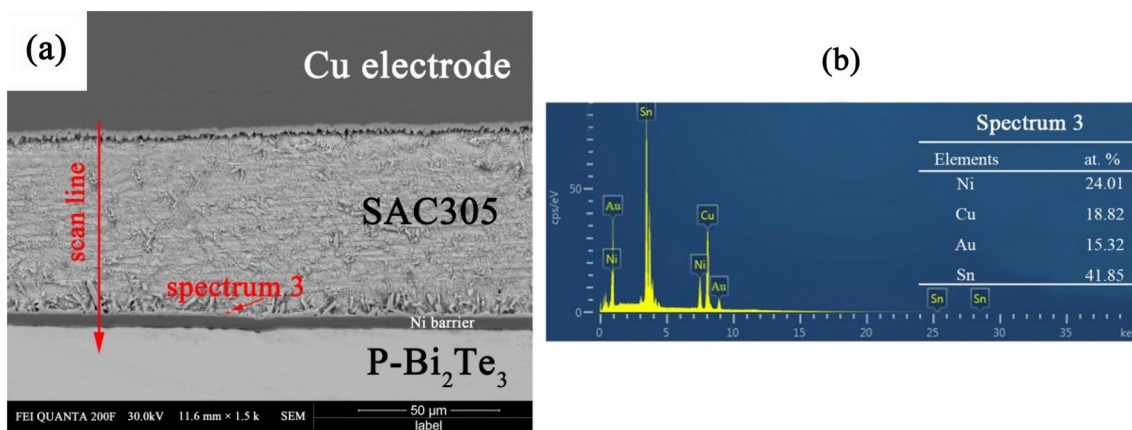

Fig. 9 **a** The cross-sectional SEM micrograph of the Cu/SAC305/Au/Ni/P-Bi$_2$Te$_3$ interface after reflow-soldering at 260 °C for 3 min; **b** The EDS result of spectrum 3
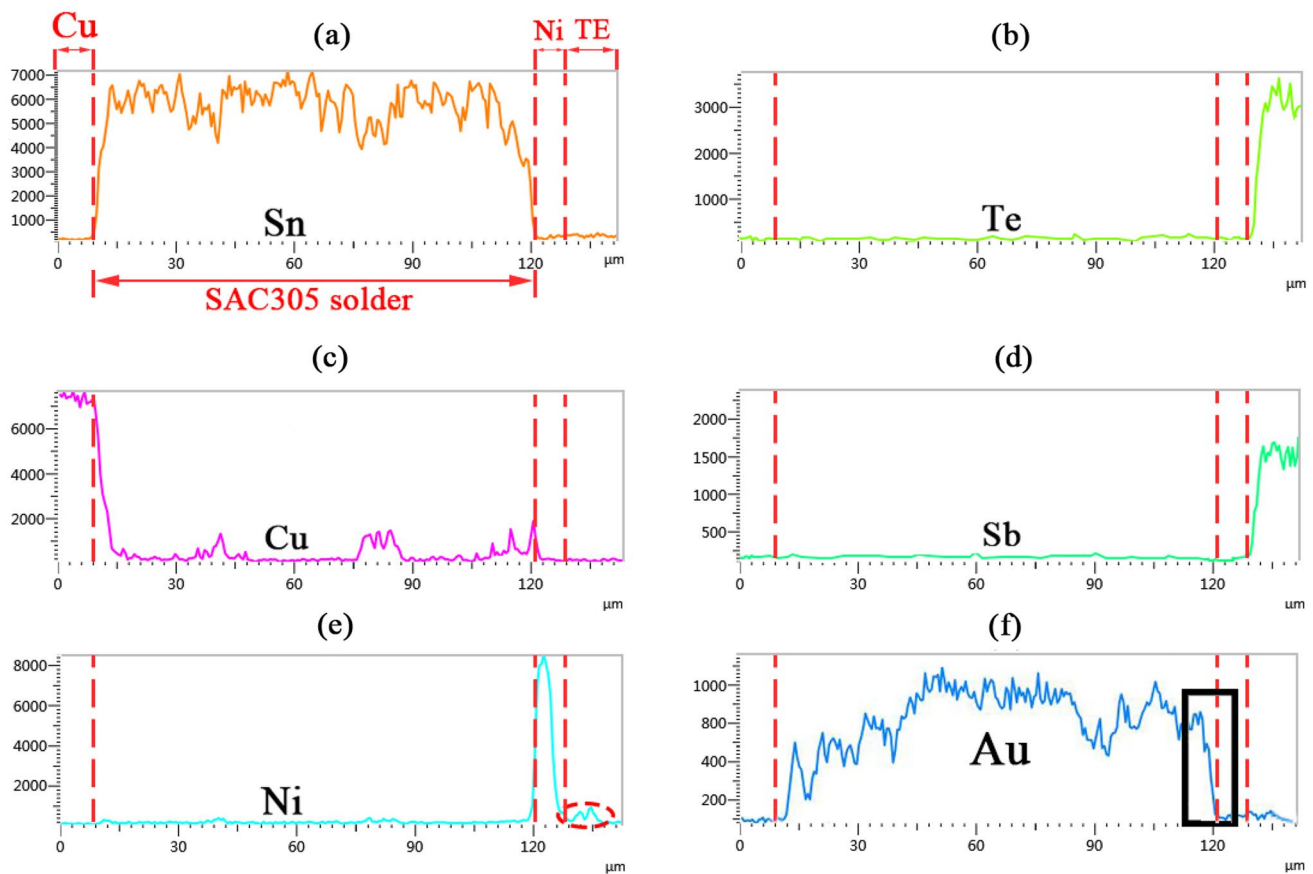
Fig. 10 Element line profiles of relative elements at the Cu/SAC305/Au/Ni/P-Bi$_2$Te$_3$ interface in Fig. 9a. **a** Sn; **b** Te; **c** Cu; **d** Sb; **e** Ni; **f** Au

at. % Cu, 15.32 at.% Au and 41. 85 at.% Sn, as shown in Fig. 9b, indicating that some Au atoms have participated in the reaction. In the Sn–Cu–Ni-Au system, Au atoms in the molten solder were confirmed to mainly react with Sn, and stable products, such as Cu$_6$Sn$_5$, Ni$_3$Sn$_4$, AuSn, etc., would aggregate adjacent to substrate and form a dense layer [52]. Furthermore, Lee et al. have demonstrated that with Au addition, a more stable interfacial microstructure with relatively slow growth rate was observed in the solder joint [53]. Figure 10 showed element line profiles of relative elements at the Cu/SAC305/Au/Ni/P-Bi$_2$Te$_3$ interface in Fig. 9a. As shown in Fig. 10a–e, the distribution of Sn, Te, Cu, Sb and Ni elements was consistence with that at the Cu/SAC305/Ni/P-Bi$_2$Te$_3$ interface, and the intensity of Ni in the P-Bi$_2$Te$_3$ at the position marked by the red oval indicated that some Ni atoms have diffused into the TE sample and formed a NiTe phase. Furthermore, as shown in Fig. 10f, the Au intensity in the solder at the position marked by the black rectangle shows Au atoms have randomly diffused into the SAC305 solder and participated in the reaction which occurred at the interface between solder and Ni barrier.

3.4 Interfacial reaction in the Cu/SAC305/N-Bi$_2$Te$_3$ couple

In Fig. 11a, the cross-sectional SEM micrograph of the Cu/SAC305/N-Bi$_2$Te$_3$ interface was established. It was significant that a very thin IMC layer with thickness of 0.5–1 μm formed at the interface between solder and N-Bi$_2$Te$_3$. According to some information reported by Chen et al., small amounts of Se elements added to Bi$_2$Te$_3$ bulk would not join the interfacial reaction, but dramatically reduce the reaction phases. Meanwhile, they suggested that this reaction phase was mainly composed of the SnTe compound [54]. Thus, it indicated that Se elements in N-Bi$_2$Te$_3$ bulk were the key factor which completely altered the reaction results in the current work. However, the question of why Se elements could efficiently inhibit the IMC growth was still interesting and needed to be further solved in the future. Figure 11b–e showed the elemental line profiles of relative elements at the Cu/SAC305/Ni/N-Bi$_2$Te$_3$ interface. As shown in Fig. 11b, after reflow-soldering at 260 °C for 3 min, it was clearly found that Sn atoms were mainly dissolved into the solder part. And
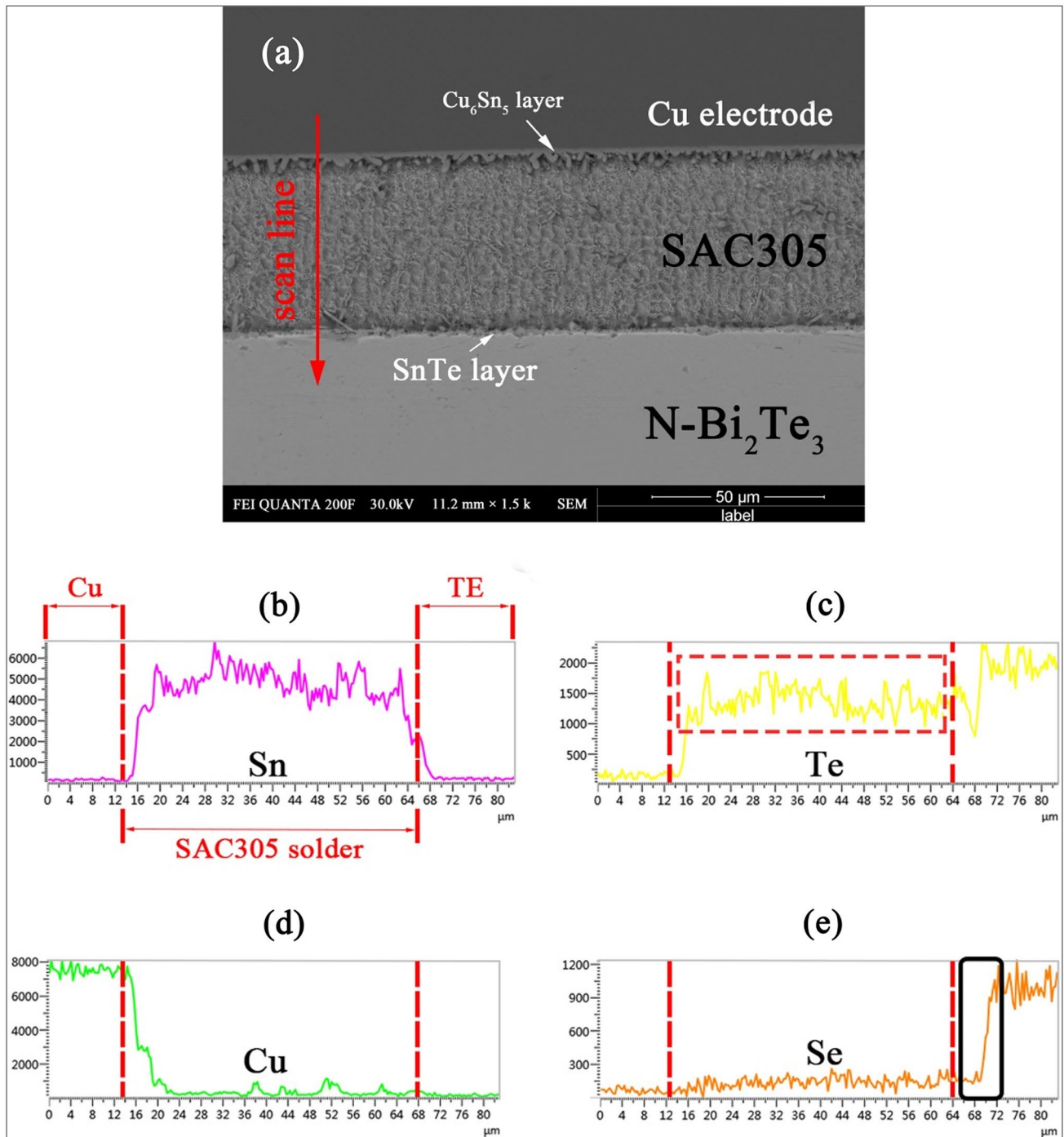
Fig. 11 **a** The cross-sectional SEM micrograph of Cu/SAC305/N-Bi$_2$Te$_3$ interface after reflow-soldering at 260 °C for 3 min; **b–e** Element line profiles of relative elements at the Cu/SAC305/Ni/N-Bi$_2$Te$_3$ interface

on N-Bi$_2$Te$_3$ side, the Sn content decreased remarkably, which confirmed that there were few Sn atoms joining the reaction at the interface between solder and N-Bi$_2$Te$_3$. However, as exhibited in Fig. 11c, the intensity of Te in the solder, which was at the position marked by the red rectangle, indicated that Te atoms have strongly diffused into

the molten solder during diffusion process. Furthermore, as shown in Fig. 11e, the Se intensity on N-Bi$_2$Te$_3$ side, which was at the position marked by the black rectangle, showed a growing tendency along the scan line. And it demonstrated that there were hardly any Se elements diffusing into the interface between solder and N-Bi$_2$Te$_3$.
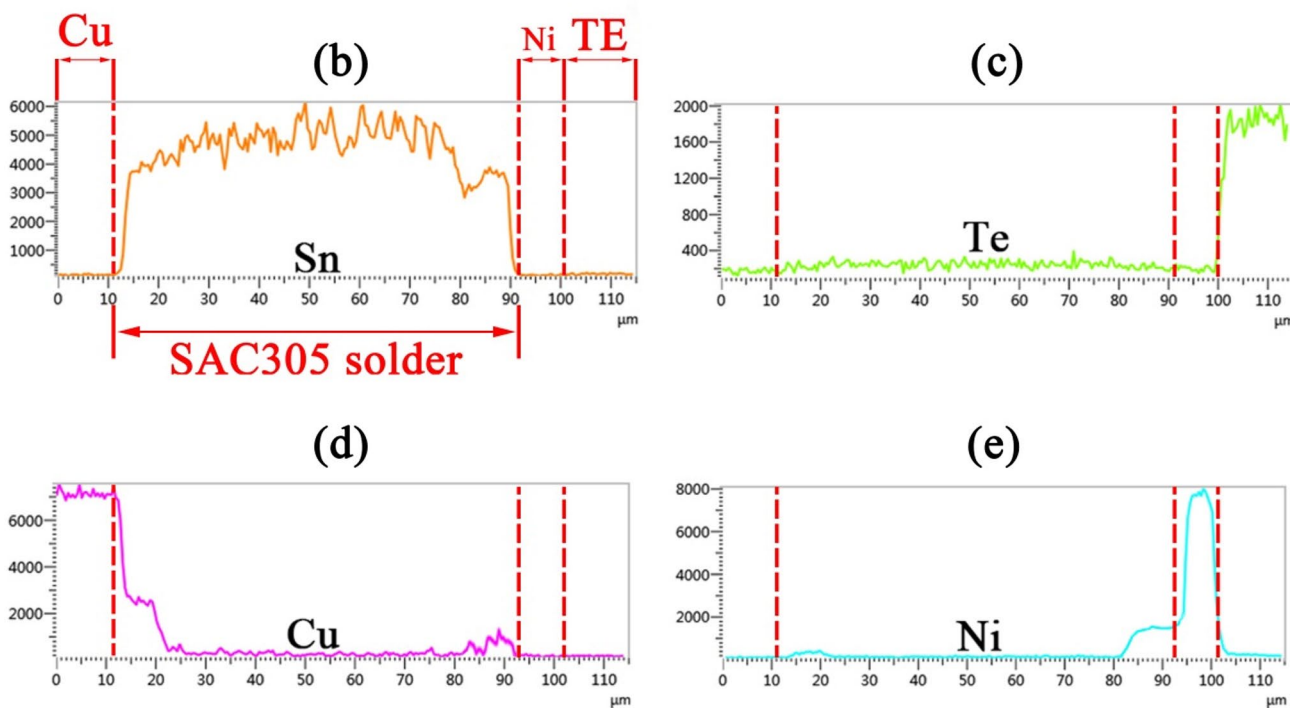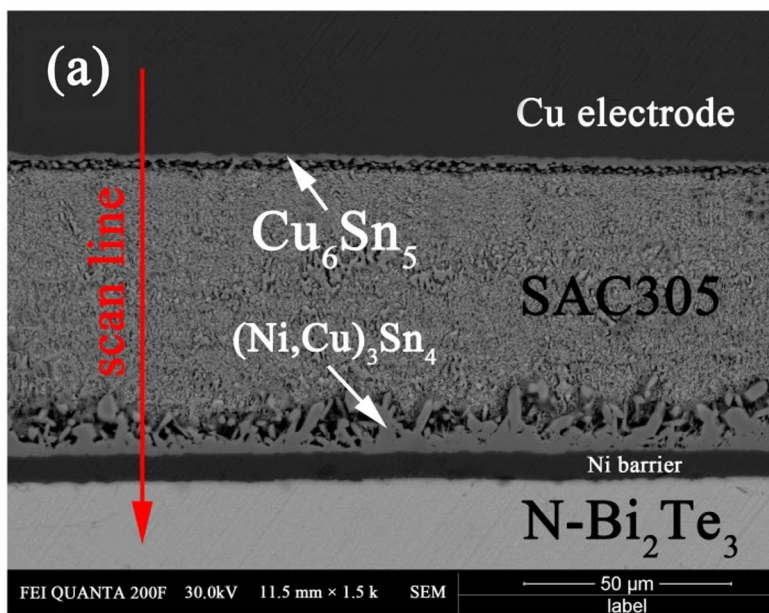
Fig. 12 **a** The cross-sectional SEM micrograph of the Cu/SAC305/Ni/N-Bi$_2$Te$_3$ interface after reflow-soldering at 260 °C for 3 min; **b–e** Element line profiles of relative elements at the Cu/SAC305/Ni/N-Bi$_2$Te$_3$ interface

3.5 Interfacial reaction in the Cu/SAC305/Ni/N-Bi$_2$Te$_3$ couple

Figure 12a exhibited the cross-sectional SEM micrograph of the Cu/SAC305/Ni/N-Bi$_2$Te$_3$ interface. At the interface between Ni barrier and SAC305 solder, the (Ni,Cu)$_3$Sn$_4$ phase appeared adjacent to Ni barrier after reflow-soldering,

and the microstructure was no difference from that of SAC305/Ni/P-Bi$_2$Te$_3$ interface. But the interface between Ni barrier and N-Bi$_2$Te$_3$, in contrast, was observed that no obvious NiTe layer formed. According to the EDS line analysis, as shown in Fig. 12e, it was detected that there were very small amount of Ni atoms diffusing into the TE sample, which suggested that there were few reactions occurring
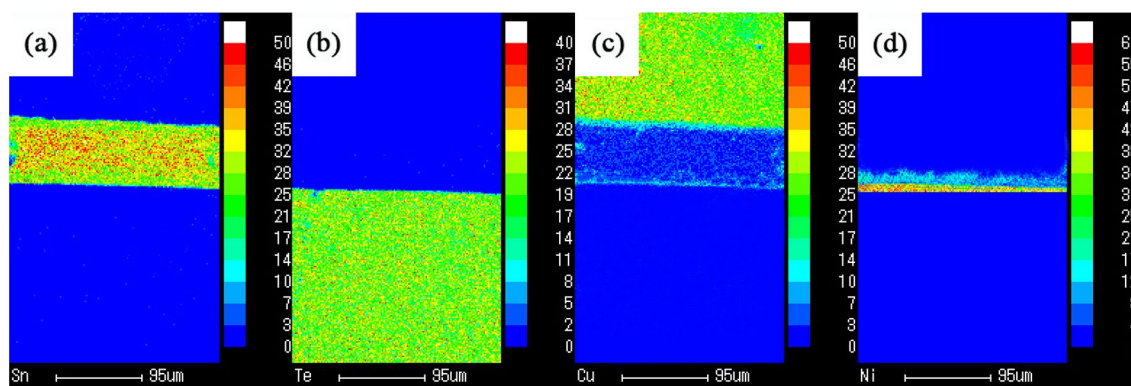
Fig. 13 EPMA results of relative elements at the Cu/SAC305/Ni/N-Bi$_2$Te$_3$ interface. **a** Sn; **b** Te; **c** Cu; **d** Ni

at the interface between Ni barrier and N-Bi$_2$Te$_3$. Further-more, EPMA results of relative elements were exhibited to determine the element distribution of bonding interface. As shown in Fig. 13a, b, under the effect of Ni barrier on inhibiting the atom diffusion, Sn atoms mainly retained in the solder while all of Te atoms retained in the N-Bi$_2$Te$_3$. Meantime, Fig. 13c indicated that Cu atoms from the elec-trode could diffuse to the molten solder during reflow-sol-dering, and preferentially reacted with Sn and Ni atoms on both sides of the SAC305 solder. Due to consumption of Ni atoms, the Ni barrier with thickness of only 3–5 μm was observed in Fig. 13d, and there were no obvious Ni atoms diffused into the N-Bi$_2$Te$_3$.

3.6 Interfacial reaction in the Cu/SAC305/Au/Ni/N-Bi$_2$Te$_3$ couple

Figure 14a showed the cross-sectional SEM micrograph of the Cu/SAC305/Au/Ni/N-Bi$_2$Te$_3$ interface after reflow-soldering at 260 °C for 3 min. Here, only Ni barrier was obsrved at the interface between solder and N-Bi$_2$Te$_3$, and the sputtering Au layer completly disappeared. Meantime, the intensity of Au in the solder at the position marked by the red rectangle, as shown in Fig. 14f, indicated that Au atoms have strongly diffused into the molten solder and participated in the reaction. In previous reports, Lee et al. has confirmed that Au additon in the Sn-based solder could react with Sn and evetually form the thermodynami-cally stable AuSn and Au$_5$Sn phases [53]. Another inves-tigation conducted by Lin et al. has detected that dendritic (Ni,Cu,Au)$_3$Sn$_4$ and scallop-shaped (Cu,Ni,Au)$_6$Sn$_5$ have formed in the solder matrix at the heat aging duration [52]. Moreover, as shown in Fig. 14d, e, the intensities of Cu and Ni in IMC layer at positions marked by the black ovals indi-cated that these two kinds of atoms have also participated in the interfacial reaction. Similar with the microstructure of IMC layer at the SAC305/Au/Ni/P-Bi$_2$Te$_3$ interface, the IMC layer at the SAC305/Au/Ni/N-Bi$_2$Te$_3$ interface was pretty

thin, which provided the further evidence that Au elements have remarkably decreased the growth rate of IMC layer.

3.7 Results of the power generation ability test

As shown in Fig. 15a, V values of three P-N modules signifi-cantly increased with increase of ΔT, suggesting that V was proportion to ΔT. According to the previous investigation, the relationship between V and ΔT could be summarized as the follow formula [55]:

$$V = (S_P - S_N) * \Delta T \tag{1}$$

where S_P and S_N denoted seebeck coefficients of P- and N-Bi$_2$Te$_3$ materials, respectively. As can be seen from Fig. 15a, with the elevation of ΔT, V values of TM$_{Ni}$ increased more dramatically than those of TM and TM$_{Ni}$/$_{Au}$. Precisely, when the ΔT increased from ~ 20 oC to ~ 90 °C, V values of TM$_{Ni}$ significantly increased from 3 mV to 18.2 mV, while those of TM increased from 3.3 mV to 12.1 mV and those of TM$_{Ni/Au}$ increased from 2.5 mV to 13.8 mV. It indicated that the fast-est rising rate led to the highest V in TM$_{Ni}$ at similar range of ΔT. In Fig. 15b, the relationship between I and ΔT was exhibited. With the increase of ΔT, I values of three kinds of modules have remarkably increased. But I_{max} of TM was measured to be 6.01 mA when ΔT was 85.2 °C, while those of TM$_{Ni/Au}$ and TM$_{Ni}$ were 7.80 mA ($\Delta T = 85.9$ °C) and 10.57 mA ($\Delta T = 85.2$ °C), respectively. Due to the value of output power (P) was calculated from V and I, and the equa-tion could be expressed as below:

$$P = V * I \tag{2}$$

In Fig. 15c, the relationship between P and ΔT was illus-trated. Obviously, in each module, the maximum value of P was obtained when ΔT reached the maximum. Typically, the P_{max} for a ΔT of 85.2 °C reached to 192.374 μW in TM$_{Ni}$.

As shown in Fig. 15d, R of TE$_{Ni/Au}$ remained stable at 4.701 mΩ, while that of TE severely increased from
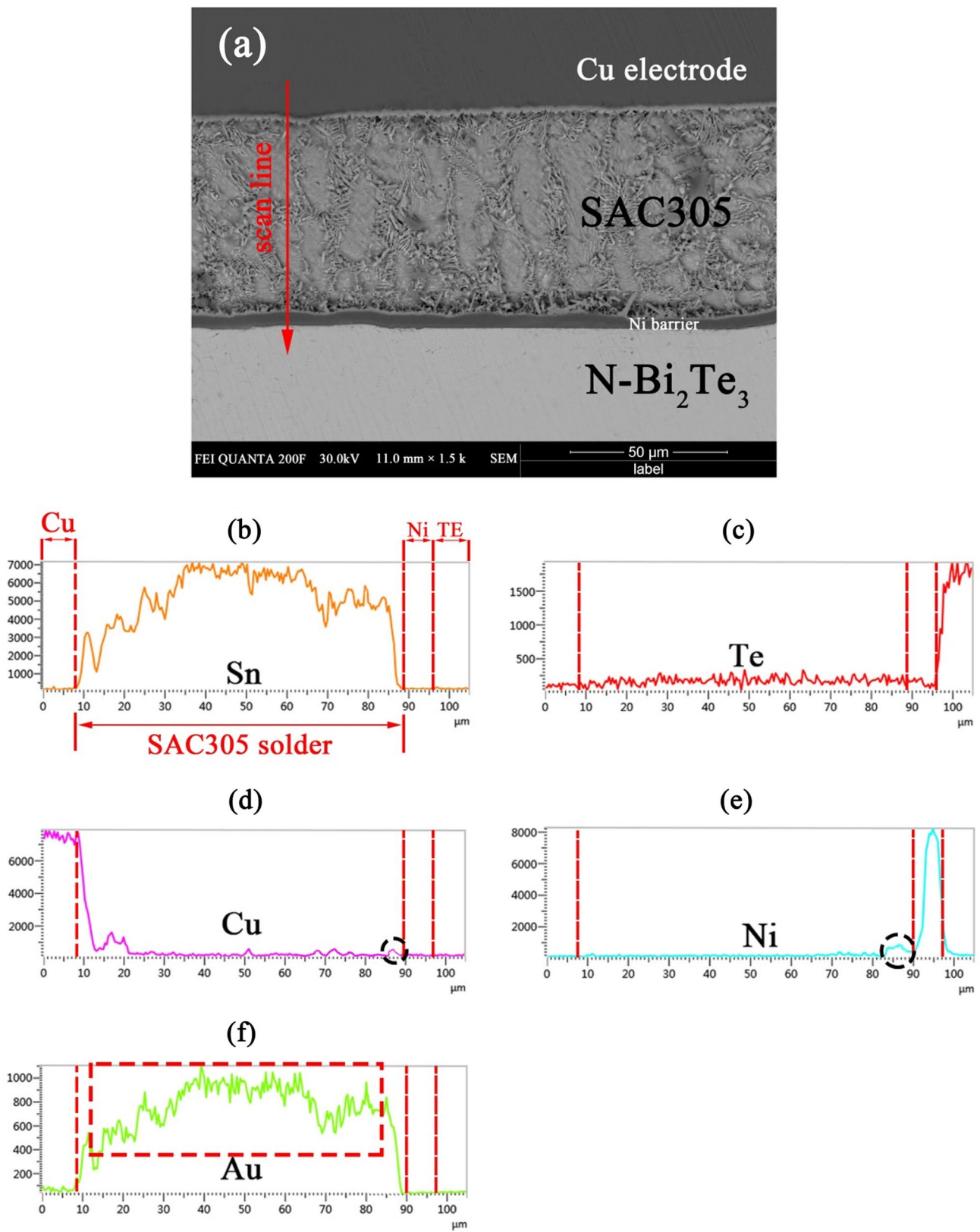
Fig. 14 **a** The cross-sectional SEM micrograph of the Cu/SAC305/Au/Ni/N-Bi_2Te_3 interface after reflow-soldering at 260 °C for 3 min; **b–f** Element line profiles of relative elements at the Cu/SAC305/Au/Ni/N-Bi_2Te_3 interface
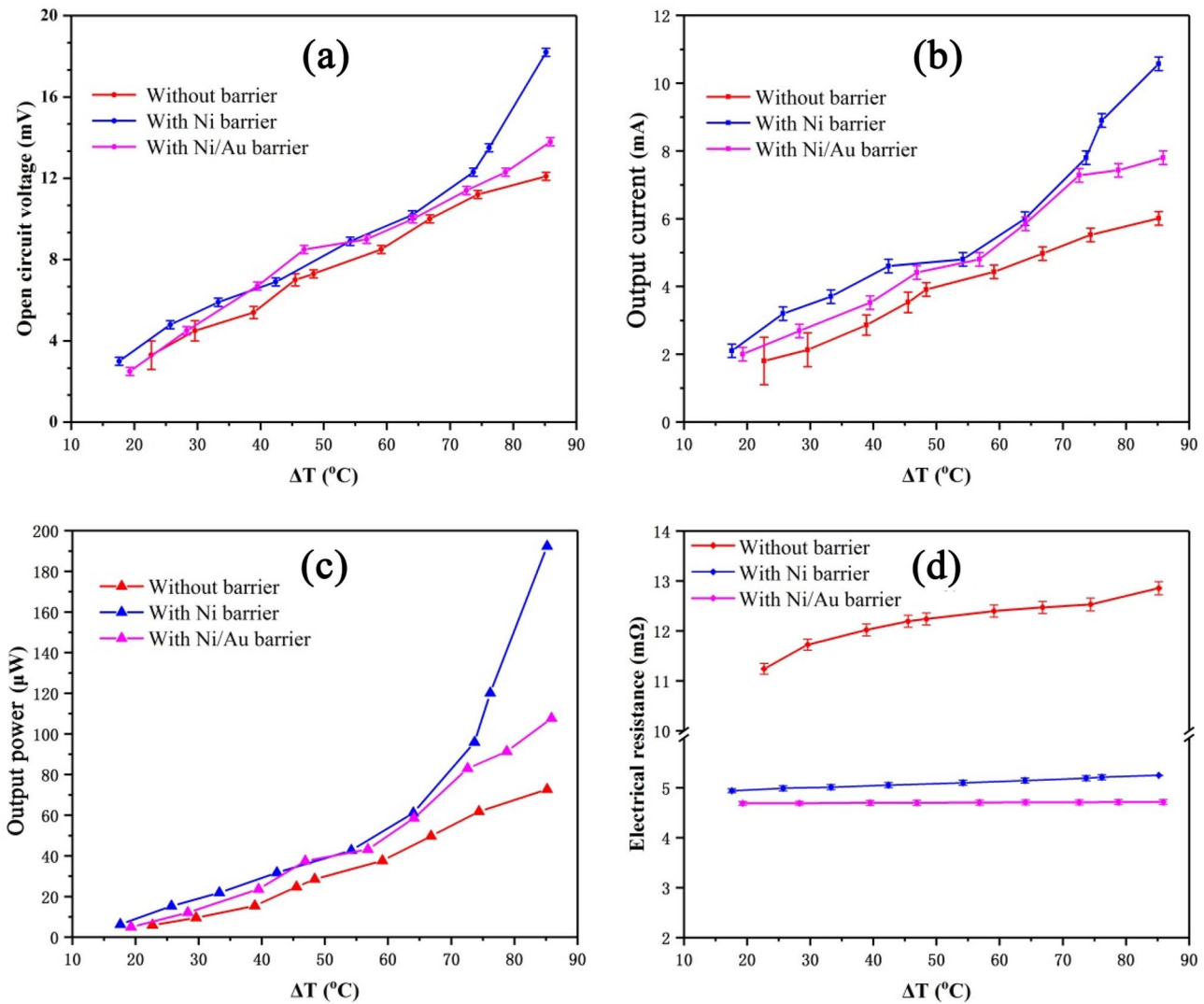
Fig. 15 Values of **a** V, **b** I, **c** P, and **d** R of three kinds of modules as function of ΔT

11.243 mΩ to 12.857 mΩ. In whole process of testing, the average R values of TM, TM_{Ni} and $TM_{Ni/Au}$ were 12.187 mΩ, 5.101 mΩ and 4.701 mΩ, respectively. Chen et al. have conducted the investigation to explore the effect of Ni barrier on TE properties of the module, and suggested that the barrier was of great important in depressing the contact resistance (R_c) of TE modules [35]. Thus in the current work, the Ni/Au barrier was suggested to be more efficient in inhibiting the IMC growth, and hence depressing the R_c value of the TE module. Commonly, with increase of R and I, the heat generated by TE module would increase. Therefore, in TM and TM_{Ni}, the open-circuit heat flow would cause underestimation of the conversion efficiency. In the Singsoog's report, the theoretical conversion efficiency (η) of one pair of the P-N module could be derived by the Eq. (3) [56]:

$$\eta = \frac{I\left[\left(S_P - S_N\right)\Delta T - IR\right]}{K\Delta T\left(S_P - S_N\right)IT_H - \frac{1}{2}I^2R} \tag{3}$$

According to research results, the S_P of P-Bi$_2$Te$_3$ was larger than the S_N of N-Bi$_2$Te$_3$, and thermal conductance (K) of both types were high value at operating temperature [35,57,58]. So, it further suggested that $TM_{Ni/Au}$ was more efficient in improving the conversion efficiency though its P value was still lower than that of TM. And our future work will involve an investigation on exploring the relation between the output power and the conversion efficiency.

4 Conclusions

In the current work, three kinds of TE modules (TM, TM_{Ni} and $TM_{Ni/Au}$) were established and tested to explore effects of Ni and Ni/Au barriers on the performance of P-N Bi_2Te_3 modules. Here, microstructures of solder joints were observed and electrical properties of modules were tested and analyzed. And some contributions of this study could be summarized as follows:

(1) At the interface between SAC305 solder and P-Bi_2Te_3, a heterogeneous IMC layer, which was composed of SnTe, SbSn, Sn and Sb phases, severely thickened during reflow-soldering. SEM results revealed that the rapid growth of IMC layer could be efficiently inhibited by Ni or Ni/Au barrier. And EDS elemental profiles also revealed that the diffusion of relative elements were suppressed by the barriers. On the other hand, due to the introduction of Ni and Au elements, compositions of IMC layers at the interface between solder and barriers completely changed. At the solder/Ni/Au/P-Bi_2Te_3 interface, the IMC layer with the more sluggish growth rate was observed, which was attributed to the effect of Au elements on decreasing the formation of IMC phases.

(2) Se elements in the N-Bi_2Te_3 sample could dramatically reduce the reaction phases, which led to a 0.5–1 µm SnTe layer forming adjacent to the N-Bi_2Te_3 sample. With the presence of barriers, microstructures and compositions of IMC layers would absolutely change. The $(Ni,Cu)_3Sn_4$ phase, as the dominated production, was detected at the interface between SAC305 solder and Ni barrier. Moreover, SEM and EDS results revealed that the IMC layer at solder/Ni/Au/N-Bi_2Te_3 interface was pretty thin, and it provided the further evidence that Au elements could remarkably decreased the growth rate of the IMC phases.

(3) According to results of the power generation ability test, due to higher values of V and I, the TM_{Ni} exhibited the higher value of P than TM and $TM_{Ni/Au}$ with increase of ΔT. On the other hand, due to lowest R value and relatively low value of I, the $TM_{Ni/Au}$ was considered to generate less heat during test process. Thus in theory, it suggested that $TM_{Ni/Au}$ was more efficient in improving the conversion efficiency.

Compliance with ethical standards

References

1. J. Jiao, C. Chen, Y. Bai, Is green technology vertical spillovers more significant in mitigating carbon intensity? Evidence from Chinese industries. J. Clean. Prod. **257**, 120354 (2020)
2. Y. Cui, S. Duan, X. Chen, X. Liu, Remarkable electronic band structure leads to high thermoelectric properties in p-type γ-Cu_2S. Vacuum **170**, 108964 (2019)
3. Du Kerui, J. Li, Towards a green world: How do green technology innovations affect total-factor carbon productivity. Energy Policy **131**, 240–250 (2019)
4. S. Budak, K. Heidary, R.B. Johnson, T. Colon, C. Muntele, D. Ila, MeV Si ion modifications on the thermoelectric generators from Si/Si + Ge superlattice nano-layered films. Appl. Surf. Sci. **310**, 221–225 (2014)
5. D. Shi, G. Wang, C. Li, X. Shen, Q. Nie, Preparation and thermoelectric properties of $MoTe_2$ thin films by magnetron co-sputtering. Vacuum **138**, 101–104 (2017)
6. MdA Al-Nimr, B. Tashtoush, A. Hasan, A novel hybrid solar ejector cooling system with thermoelectric generators. Energy **198**, 117318 (2020)
7. Y. Kiyota, T. Kawamoto, T. Mori, Low-temperature properties of thermoelectric generators using molecular conductors. Synth. Met. **259**, 116217 (2020)
8. H. Khalil, H. Hamdy, Enhancement thermoelectric generators output power from heat recovery of chimneys by using flaps. J. Power Sources **443**, 227266 (2019)
9. Y. Tian, Z. Miao, X. Meng, W. Yan, M. Zhu, Thermo-mechanical analysis of thermoelectric devices based on single p-n pair. Energy Procedia **158**, 1559–1564 (2019)
10. J.M.C. Garrido, J.M. Silveyra, Virtual prototype of a low-cost vacuum baffle based on thermoelectric cooling. Vacuum **151**, 156–162 (2018)
11. M. Marefati, M. Mehrpooya, Introducing a hybrid photovoltaic solar, proton exchange membrane fuel cell and thermoelectric device system. Sustain. Energy Technol. Assess. **36**, 100550 (2019)
12. S. Ferhat, C. Domain, J. Vidal, D. Noël, B. Ratier, B. Lucas, Flexible thermoelectric device based on $TiS_2(HA)_x$ n-type nanocomposite printed on paper. Org. Electron. **68**, 256–263 (2019)
13. Qu Sanyin, Y. Chen, W. Shi, M. Wang, Q. Yao, L. Chen, Cotton-based wearable poly(3-hexylthiophene) electronic device for thermoelectric application with cross-plane temperature gradient. Thin Solid Films **667**, 59–63 (2018)
14. Y. Yin, B. Tudu, A. Tiwari, Recent advances in oxide thermoelectric materials and modules. Vacuum **146**, 356–374 (2017)
15. V. Shalini, M. Navaneethan, S. Harish, J. Archana, S. Ponnusamy, H. Ikeda, Y. Hayakawa, Design and fabrication of PANI/GO nanocomposite for enhanced room-temperature thermoelectric application. Appl. Surf. Sci. **493**, 1350–1360 (2019)
16. T. Torfs, V. Leonov, C. Van Hoof, B. Gyselinckx, Body-heat powered autonomous pulse oximeter. Sensors (2006). https://doi.org/10.1109/ICSENS.2007.355497
17. N. Jaziri, A. Boughamoura, J. Müller, B. Mezghani, F. Tounsi, M. Ismail, A comprehensive review of thermoelectric generators: technologies and common applications. Energy Rep. (2019). https://doi.org/10.1016/j.egyr.2019.12.011

18. D. Luo, R. Wang, Yu Wei, Z. Sun, X. Meng, Theoretical analysis of energy recovery potential for different types of conventional vehicles with a thermoelectric generator. Energy Procedia **158**, 142–147 (2019)

19. R. Ramírez, A.S. Gutiérrez, J.J.C. Eras, B. Hernández, J.D. Forero, Data supporting the evaluation of the energy recovery potential of thermoelectric generators in diesel engines. Data Brief **28**, 105075 (2020)

20. W.B. Nader, Thermoelectric generator optimization for hybrid electric vehicles. Appl. Therm. Eng. **167**, 114761 (2020)

21. L. Wang, X. Jia, D. Wang, G. Zhu, J. Li, Preparation and thermoelectric properties of polythiophene/multiwalled carbon nanotube composites. Synth. Met. **18**, 79–85 (2013)

22. G.-H. Kim, L. Shao, K. Zhang, K.P. Pipe, Engineered doping of organic semiconductors for enhanced thermoelectric efficiency. Nat. Mater. **12**, 19–23 (2017)

23. Y. Zhu, C. Wang, H. Wang, W. Su, J. Liu, J. Li, Influence of Dy/Bi dual doping on thermoelectric performance of CaMnO3 ceramics. Mater. Chem. Phys. **144**, 385–389 (2014)

24. S.M. Pourkiaei, M.H. Ahmadi, M. Sadeghzadeh, S. Moosavi, F. Pourfayaz, L. Chen, MdAP Yazdi, R. Kumar, Thermoelectric cooler and thermoelectric generator devices: a review of present and potential applications, modeling and materials. Energy **186**, 115849 (2019)

25. J.-S. Rhyee, K.H. Lee, S.M. Lee, E. Cho, S. Kim II, E. Lee et al., Peierls distortion as a route to high thermoelectric performance in In$_4$Se$_{3-d}$ crystals. Nature **459**, 965–968 (2009)

26. L.-D. Zhao, S.-H. Lo, Y. Zhang, H. Sun, G. Tan, C. Uher et al., Ultralow thermal conductivity and high thermoelectric figure of merit in SnSe crystals. Nature **508**, 373–377 (2014)

27. K. Ahmad, C. Wan, M.A. Al-Eshaikh, A.N. Kadachi, Enhanced thermoelectric performance of Bi$_2$Te$_3$ based graphene nanocomposites. Appl. Surf. Sci. **474**, 2–8 (2019)

28. O. Ivanov, M. Yaprintsev, Variable-range hopping conductivity in Lu-doped Bi$_2$Te$_3$. Solid State Sci. **76**, 111–117 (2018)

29. Y. Liu, M. Zhou, J. He, Towards higher thermoelectric performance of Bi2Te3 via defect engineering. Scr. Mater. **111**, 39–43 (2016)

30. M. Tan, Y. Deng, Y. Wang, Ordered structure and high thermoelectric properties of Bi2(Te, Se)3 nanowire array. Nano Energy **3**, 144–151 (2014)

31. R. Venkatasubramanian, E. Silvola, T. Colpitts, B. O'Quinn, Thin-film thermoelectric devices with high room-temperature figures of merit. Mater. Sustain. Energy 120–125 (2010)

32. H. Wang, X. Hu, X. Jiang, Effects of Ni modified MWCNTs on the microstructural evolution and shear strength of Sn-3.0Ag-0.5Cu composite solder joints. Mater. Charact. **163**, 110287 (2020). https://doi.org/10.1016/j.matchar.2020.110287

33. Xu Zhiwu, Z. Li, D. Zhao, X. Liu, J. Yan, Effects of Zn on intermetallic compounds and strength of Al/Mg joints ultrasonically soldered in air. J. Mater. Process. Technol. **271**, 384–393 (2019)

34. Z. Zhipeng, Z. Xiaomin, Wu Tan Shulin, Z.H. Zhouzhi, Growth of intermetallic compounds in solder joints based on strongly coupled thermo–mechano–electro–diffusional theory. Microelectron. Reliab. **107**, 113621 (2020)

35. L. Chen, D. Mei, Y. Wang, Y. Li, Ni barrier in Bi$_2$Te$_3$-based thermoelectric modules for reduced contact resistance and enhanced power generation properties. J. Alloys Compd. **769**, 314–320 (2019)

36. Z. Zhang, Hu Xiaowu, X. Jiang, Y. Li, Influences of mono-Ni(P) and dual-Cu/Ni(P) plating on the interfacial microstructure evolution of solder joints. Metall. Mater. Trans. A **50**, 480–492 (2019)

37. J. Cheng, Hu Xiaowu, Z. Zhang, Q. Li, Effects of the Ni(P) plating thickness on microstructure evolution of interfacial IMCs in Sn–58Bi/Ni(P)/Cu solder joints. J. Mater. Sci. (2020). https://doi.org/10.1007/s10854-020-03695-y

38. H.-C. Hsieh, C.-H. Wang, W.-C. Lin, S. Chakroborty, T.-H. Lee, H.-S. Chu, A.T. Wu, Electroless Co-P diffusion barrier for n-PbTe thermoelectric material. J. Alloys Compd. **728**, 1023–1029 (2017)

39. X. Ren, W. Zheng, H. Qiao, L. Ren, S. Liu, Z. Huang, X. Qi, Z. Wang, J. Zhong, H. Zhang, Enhanced photoresponse behavior of Au@Bi$_2$Te$_3$ based photoelectrochemical-type photodetector at solid-solid-liquid joint interface. Mater. Today Energy **16**, 100401 (2020)

40. H. Zhang, F. Ye, Hu Yangsen, J. Liu, Y. Zhang, Wu Yigui, Hu Zhiyu, The investigation of thermal properties on multilayer Sb$_2$Te$_3$/Au thermoelectric material system with ultra-thin Au interlayers. Superlattices Microstruct. **89**, 312–318 (2016)

41. J.L. Cui, W.J. Xiu, L.D. Mao, P.Z. Ying, L. Jiang, X. Qian, Thermoelectric properties of Ag-doped n-type (Bi2Te3)09–(Bi$_{2-x}$Ag$_x$Se$_3$)$_{0.1}$(x=0–0.4) alloys prepared by spark plasma sintering. J. Solid State Chem. **180**, 1158–1162 (2007)

42. H. Choi, K. Jeong, J. Chae, H. Park, J. Baeck, T.H. Kim, J.Y. Song, J. Park, K.-H. Jeong, M.-H. Cho, Enhancement in thermoelectric properties of Te-embedded Bi$_2$Te$_3$ by preferential phonon scattering in heterostructure interface. Nano Energy **47**, 374–384 (2018)

43. J. Cheng, X. Hu, Q. Li, Influence of Ni and Cu electrodeposits on the interfacial reaction between SAC305 solder and the Bi2(Te, Se)3 thermoelectric material. J. Mater. Sci. **30**, 14791–14804 (2019)

44. K.H. Prakash, T. Sritharan, Interface reaction between copper and molten tin–lead solders. Acta Mater. **49**, 2481–2489 (2001)

45. C.-H. Lee, W.-T. Chen, C.-N. Liao, Effect of antimony on vigorous interfacial reaction of Sn–Sb/Te couples. J. Alloys Compd. **509**, 5142–5146 (2011)

46. J. Cheng, X. Hu, Q. Li, Effects of the Ni electrodeposit on microstructure evolution and electrical resistance of the P-type Bi$_2$Te$_3$ solder joint. J. Alloys Compd. **832**, 155006 (2020)

47. A.M. Gusak, K.N. Tu, C. Chen, Extremely rapid grain growth in scallop-type Cu$_6$Sn$_5$ during solid–liquid interdiffusion reactions in micro-bump solder joints. Scr. Mater. **179**, 45–48 (2020)

48. Z. Zhao, J. Shang, Hu Anmin, M. Li, The effects of Sn solder grain size on the morphology and evolution of Cu$_6$Sn$_5$ in the aging process. Mater. Lett. **185**, 92–95 (2016)

49. K.-K. Wang, D. Gan, K.-C. Hsieh, The orientation relationships of the Cu$_3$Sn/Cu interfaces and a discussion of the formation sequence of Cu$_3$Sn and Cu$_6$Sn$_5$. Thin Solid Films **562**, 398–404 (2014)

50. S.-W. Chen, S.-H. Wu, S.-W. Lee, Interfacial reactions in the Sn-(Cu)/Ni, Sn-(Ni)/Cu, and Sn/(Cu, Ni) systems. J. Electron. Mater. **32**, 1188–1194 (2003)

51. E. Yusufu, T. Sugahara, M. Okajima, S. Nambu, K. Suganum, Effects of microstructure of Ni barrier on bonding interface diffusion behaviors of Bi–Te-based thermoelectric material. J. Alloys Compd. **817**, 152731 (2020)

52. H.-J. Lin, J.-S. Lin, T.-H. Chuang, Electromigration of Sn–3Ag–0.5Cu and Sn–3Ag–0.5Cu–0.5Ce–0.2Zn solder joints with Au/Ni(P)/Cu and Ag/Cu pads. J. Alloys Compd. **487**, 458–465 (2009)

53. B.-S. Lee, Y.-H. Ko, J.-H. Bang, C.-W. Lee, S. Yoo, J.-K. Kim, J.-W. Yoon, Interfacial reactions and mechanical strength of Sn-3.0Ag-0.5Cu/Ni/Cu and Au-20Sn/Ni/Cu solder joints for power electronics applications. Microelectron. Reliab. **71**, 119–125 (2017)

54. S.-W. Chen, C. Wu, H. Wu, W.-T. Chiu, Interfacial reactions in Sn/Bi$_2$Te$_3$, Sn/Bi$_2$Se$_3$ and Sn/Bi$_2$(Te$_{1-x}$Se$_x$)$_3$ couples. J. Alloys Compd. **611**, 313–318 (2014)

55. H.-J. You, H.-S. Chu, W.-J. Li, W.-L. Lee, Influence of different substrate materials on thermoelectric module with bulk legs. J. Power Sources **438**, 227055 (2019)

56. K. Singsoog, T. Seetawan, Effecting the thermoelectric properties of p-MnSi$_{1.75}$ and n-Mg$_{1.98}$Ag$_{0.02}$Si module on power generation. Phys. B **566**, 1–5 (2019)

57. H. Wu, B.-Y. Chen, H.-Y. Cheng, The p-n conduction type transition in Ge-incorporated Bi$_2$Te$_3$ thermoelectric materials. Acta Mater. **122**, 120–129 (2017)

58. H. Mamur, M.R.A. Bhuiyan, F. Korkmaz, M. Nil, A review on bismuth telluride (Bi$_2$Te$_3$) nanostructure for thermoelectric applications. Renew. Sustain. Energy Rev. **82**, 4159–4169 (2018)